Generating Synthetic µCT Images of Wood Fibre Materials

Erik L.G. Wernersson, Cris L Luengo Hendriks, Anders Brun
Centre for Image Analysis
Box 337, SE-751 05 Uppsala, Sweden
{erikw, cris, anders}@cb.uu.se

Abstract

X-ray Computerized Tomography at micrometer resolution (µCT) is an important tool for understanding the properties of wood fibre materials such as paper, carton and wood fibre composites. While many image analysis methods have been developed for µCT images in wood science, the evaluation of these methods if often not thorough enough because of the lack of a dataset with ground truth.

This paper describes the generation of synthetic µCT volumes of wood fibre materials. Fibres with a high degree of morphological variations are modeled and densely packed into a volume of the material. Using a simulation of the µCT image acquisition process, realistic synthetic images are obtained. This simulation uses noise characterized from a set of µCT images. The synthetic images have a known ground truth, and can therefore be used when evaluating image analysis methods.

1. Introduction and Related Work

One common method in material sciences is analysis of micrographs. Micrographs, or microscope images, used to be analyzed manually, but computerized image analysis is becoming increasingly important because of the accuracy and objectivity of the measurements it yields. With the advent of 3D microscopic imaging (µCT, confocal microscopy, etc.), manual analysis is no longer possible. For each new material studied, however, it is often necessary to adapt existing image analysis programs or create completely new methods. Such new or modified methods need to be evaluated before their results can be trusted. For proper evaluation, a ground truth or gold standard is necessary. Because this is typically unavailable for image data, synthetic images are often the only way to evaluate programs. These synthetic images are, however, always simplified versions of real images, and sometimes simplified so much that they do not properly evaluate the methods. One of the more important features of µCT images is the correlated noise, described as artefacts. This correlation is often ignored in algorithm evaluations.

Here we propose a method of generating synthetic images of wood fibre composites as imaged through µCT. The synthetic images contain realistic wood fibres with high degree of morphological variation, and by simulating the image acquisition process, we introduce several artefacts observed in µCT images. These synthetic images are much more realistic than any used so far in the literature.

Many methods in the literature could be evaluated in some way using our simulator. It could be used to determine what kind of fibres that the tracking method in [2] is able to follow and when it fails. Ground truth images could be used to evaluate the anisotropic diffusion method used to denoise tomograms in [6] as well as the following seeded region growing segmentation method that is used to classify fibre material, filler and air. Error bonds could be estimated for the method of calculating *relative bonded area* in [11] and also for the different measurements on fibres presented in [15]. Another usage is to study what happens when methods designed for other modalities are applied to µCT volumes. Methods that might work well on CT images are for example the MSER-based tracking method in [5] used on images of microtomes and the 2D segmentation method used on SEM images presented in [1].

Wang and Shaler describe a method to simulate volumes of wood fibre composites using certain global parameters such as density [17]. They use straight fibres with constant thickness, and do not simulate fibre packing. Faessel et al. [8] generate 3D fibre volumes by placing fibres randomly. Fibres are placed one by one, independently of what is already in the volume, and, thus, they can intersect each other. The fibres have circular cross sections and are characterized by a position, angle, length and radius. The volume generation is steered by the volume fraction of fibre material.

A noise generator for cone beam CT images is described by Tu et al. in [16], where noise of three kinds is added: quantum noise (photon count fluctuations), detector blurring, and additive system noise (to simulate scintillator and CCD). The quantum noise and additive system noise are Gaussian, and the detector blurring is simulated by convolving the projections with a Gaussian kernel.

We use a similar µCT simulation, but it uses parallel beam with filtered back projection. In addition to the noise used by the simulator of Tu et al., we add correlated fluctuations of the X-ray beam over time, and simulate phase effects, detector element variation and partial volume effects.

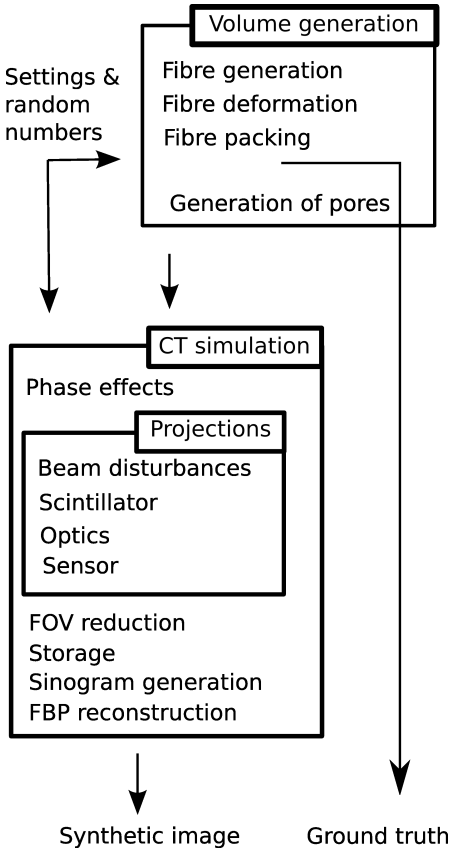

Figure 1. Scheme of the process.

The following sections describe the various parts of our simulator (see Fig. 1): the generation of the fibres and their placement in a volume, the generation of projections and noise, phase effects, and the reconstruction of the volumetric image.

2 Generation of Synthetic Fibre Volumes

The first step in the simulation process is to create a volumetric model, a phantom, of the fibre material. To make the voxel representation accurate, so called partial volume effects are taken into account. This means that each voxel store information about the average properties of the material inside it.

2.1 Modeling Individual Fibres

Fibres are individually shaped from a set of random variables that are uniformly distributed. Cross sections of the fibress are modelled using superellipses,

$$((x/r_1)^n + (y/r_2)^n)^{1/n} = 1.$$

The parameters of this cross section are randomly selected for each fibre, drawn from uniform distributions. The wall thickness of a fibre is modeled by a uniformly distributed random variable t. Some realizations of these superellipse cross sections can be seen in Fig. 2.

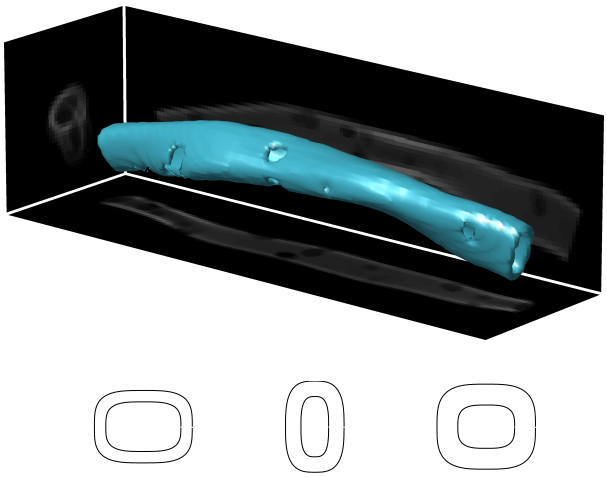

Figure 2. Top: One synthetic fibre. Bottom: Three realizations of fibre cross sections based on superellipses.

The length of a fibre is modeled by L. To make the fibre more irregular, the fibre is both twisted and bent. The twist of the cross section is modeled by a smooth rotation along the fibre axis of a total of f radians. The fibre is also bent along its axis around a circle with the radius R.

To account for the fine structure of the fibre surface, Perlin noise [13] was used to deform the fibre surface. It has the following properties:

- narrow bandpass,
- statistical invariance under rotation and,
- statistical invariance under translation.

This process is often used in computer graphics to model natural materials like wood, marble and rusty surfaces. In this context it inserts random dents and bumps in the fibre surface. Pores, holes perforating the fibre wall, are also inserted randomly in a separate process.

2.2 Packing Fibres

In the present version of the simulator, the fibres are packed into a volume using a relatively simple procedure. It places each fibre inside the volume at a random position where it does not cover any other fibre. The fibre is then shifted by random steps in the two directions perpendicular to the fibre direction until it either reaches the border of the volume or hits another fibre. In this manner, all fibres will eventually have contact with each other.

2.3 Generating Ground Truth Data

The phantom allows us to extract ground truth volume datasets. We can for instance generate a noiseless volume that can later be used to validate a reconstruction or filtering algorithm. Another option is to output a ground truth

segmentation of the fibres, perfectly labeling each fibre individually, which can be used to validate segmentation algorithms.

3. µCT Simulation

The second step in the simulation process is to model the sample being scanned and reconstructed by computerized tomography. The goal of the simulator is to introduce realistic artifacts, not a complete simulation of the physics of any specific µCT setup.

There are many artefacts inherent with CT imaging, for example ringing around edges, ring artefacts, streaks, etc. An example of ringing can be seen in the close-up on a fibre cross section, and a weak ring artefact can be seen in a tomogram shown in Fig. 3.

We have used images from the TOMCAT [7] beam line at the Paul Scherrer Institut (PSI) in Villigen, Switzerland to estimate realistic noise levels, and we have also chosen to use the same bit depth in our projections as their detector system has, 14 bit. The real images were recorded using 8 keV beam energy and a magnification giving a voxel size of $0.7\mu m$ in the reconstructions.

CT imaging is based on the Radon transform [9] :

$$I(x,y) = I_0(x,y)\exp\left\{-\int \mu(x,y,z)\mathrm{d}z\right\}, \qquad (1)$$

where I_0 is the incoming intensity to the sample, I is the received intensity at the detector, $\mu(x,y,z)$ is the attenuation of the sample, which is set up so that the incoming rays travel parallel in the z-direction. The goal is to reconstruct $\mu(x,y,z)$ from a number of projections or Radon transforms of a sample.

We use the Radon transform function in MATLAB, which returns P_θ:

$$P_\theta(x,y) = \int \mu_\theta(x,y,z)\mathrm{d}z, \qquad (2)$$

when the sample is rotated θ degrees. Taking μ normalized to the interval $[0,1]$, $P_\theta(x,y)$ will be in the range $[0,M]$, where M is given by the size of the volume along the z-axis. To transform a projection from eq. 2 to the form of eq. 1 we introduce:

$$\begin{aligned}\hat{P}_\theta &= I_0\exp\{-kP_\theta\}\\ &= I_0\exp\{-k\int_\tau \mu_\theta(x,y,z)\mathrm{d}z\}\\ &\in [I_0\exp\{-kM\}, I_0],\end{aligned}$$

where

$$I_0 = 2^{14} - k_m,$$
$$k = -\frac{1}{M}\log\left(\frac{k_m}{I_0}\right).$$

The constant k_m is introduced to protect against overflow of the dynamic range when disturbances are introduced in I_0. With the settings above, we get:

$$\hat{P}_\theta \in [k_m, 2^{14} - k_m].$$

At this step the projection is discretized to 14 bits, simulating what a sensor registers. The next step is to calculate $P_\theta(x,y)$ for each angle and then construct the sinograms before doing a reconstruction. We get back a truncated (due to the discretisations) version of P, $\bar{P}$ by:

$$\bar{P}_\theta(x,y) = -\log\left(\frac{\hat{P}_\theta(x,y)}{I_0}\right)\frac{1}{k}. \qquad (3)$$

Within the sample, not only the attenuation coefficient changes, but also the refractive index. This complicates the process slightly, and would require a complex transfer function to model. However, it can be shown [4] that the effects of this phenomenon are approximated in a simple way by replacing μ_θ in eq. 2 by

$$o_\theta(x,y,z) := \mu_\theta(x,y,z) + D\Delta n_\theta(x,y,z). \qquad (4)$$

where $n(x,y,z)$ is the real part of the refractive index, $D(x,y,z)$ is the distance to the sensor and

$$\Delta = (\partial^2/\partial x^2 + \partial^2/\partial y^2 + \partial^2/\partial z^2),$$

is the Laplace operator.

The number of projections M_p is set to

$$M_p = \frac{\pi}{2}N_r,$$

where N_r is the number of rays. This is arguably the optimal choice, see [9].

Finally, sinograms are generated and the filtered back projection method [9] is used to reconstruct the image function.

3.1. Sensor Noise

Using five images from PSI, acquired when the beam was blocked, it is estimated that the sensor has approximately normally distributed uncorrelated noise with mean value $\mu_{sensor} = 397$ and standard deviation $\sigma_{sensor} = 14$. Such noise is synthesized and added for each $\hat{P}_\theta$.

3.2. Beam, Optics and Scintillator

The beam noise is characterized using ten consecutive images from PSI, taken at the same speed rate as the projection images, without a sample in the beam path.

If we remove the average offset from these images, uncorrelated noise remains with an approximately normal distribution and a standard deviation of $\sigma_{total} = 215$.

Since

$$\sigma^2_{total} = \sigma^2_{sensor} + \sigma^2_{beam},$$

$\sigma_{beam} = 214.5$ and hence the sensor noise is small but not negligible for the total noise. The beam noise is synthetisized and added to each I_0.

The optical system and sensor is assumed to have a Gaussian point spread function, we introduce this in eq. 3 by letting

$$\hat{P}_\theta := \hat{P}_\theta * G(0,\Sigma),$$

where $*$ denotes convolution and $\Sigma = \mathrm{diag}(\sigma_{psp}, \sigma_{psp})$.

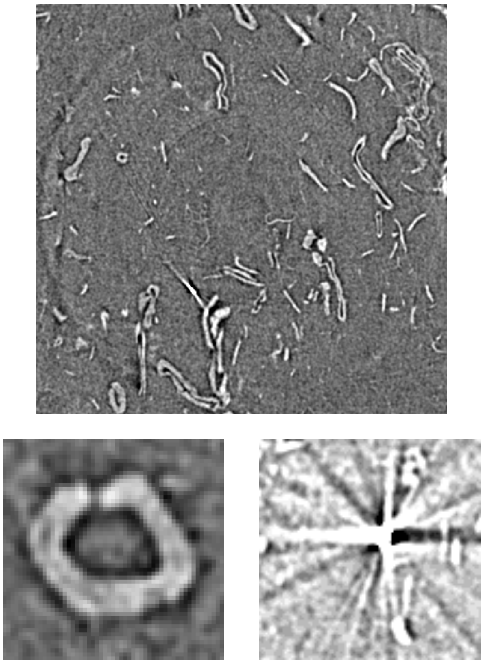

Figure 3. Examples of real data. Top: A ring shaped artefact. Left: ringing. Right: Hard object.

3.3. Mean Intensity

The mean intensity varies due to top-up injections in the synchrotron storage ring. From a series of 1500 projections, an area of 10,000 pixels from the detector (not occluded by the mounted sample) was cut out and the mean value for each projection was stored. The mean intensity varies slightly from projection to projection and has a variance of 42.

The auto-correlation function is sinusoidal with a period of 26. It is also exponentially decreasing and can thus be modeled by an autoregressive (AR) model [10]. We estimate an AR(26)-process that has the form

$$\sum_{k=0}^{25} a_k m(t-k) = e(t-k),$$

where $e(t) \in N(0,1)$. Simulations of this model reveal a behavior that is very similar to the time series of measured mean values. Together with the noise found under the last heading, the full expression for the beam intensity is:

$$I_0(x,y,t) = 2^{14} - k_m + m(t) + N(0,\sigma_{beam}).$$

3.4. Ring Artefacts

Ring-shaped artefacts are introduced when the response function of one detector element deviates from that of its neighbors. Within the simulator, all pixels in the detector are initialized to have the same linear transfer function but before the first projection, the array is distorted. One pixel in each detector row is randomly chosen and the slope of its transfer function is multiplied with a value $k \in N(1,\sigma_p)$.

The strenght of ring artefacts can to some degree be reduced; either in the sinograms as in [14, 12] or in the spatial domain as a post-processing filter, see [3].

3.5. Hard Objects and Air Bubbles

Small and highly scattering or absorbing pieces of metal are present in some of our imaged samples. Such pieces completely block the light, causing the measured intensity to deviate from the CT model. Additionally, scattering by these metal pieces increases the intensity values at other locations in the projection. Small objects with a high attenuation are added to the artificial volumes by randomly inserting high values in $\mu(x,y,z)$. Doing so cause occlusion but will not cause any scattering in the simulations.

3.6. Reduced Field of View

The projections are incomplete when some parts of the sample is outside of the field of view. This might be intentional when using local tomography to look inside a large sample; but might also be accidental, and happen when for example imaging paper material where a few fibres point out of the sample. This behavior is modeled in the simulator by removing r_{FOV} pixel lines from each side of the projection data.

4. Implementation and Experiments

The implementation is done in MATLAB where also the AR model parameters are estimated using the System Identification Toolbox.

Equation 4 is simplified by letting D be constant. We also replace the refractive index n by the attenuation coefficient, μ. That gives the simplified expression:

$$D\Delta n_\theta(x,y,z) \approx S_p \mu_\theta(x,y,z) * \text{DoG},$$

which is used where S_p is a constant and DoG is a *Difference of Gaussians*.

To generate a volume of size $200 \times 200 \times 200$ with fibres densely packed takes a few hours on a PC (8GB RAM, Intel Xeon E5340). The following CT simulation of the volume takes less than an hour using the settings in Table 1.

An isosurface of a synthetic volume can be seen in Fig. 5a and a cross section in Fig. 4, left. The same volume is shown in Figs. 4, right and 5b after passing through the μCT simulation pipeline described in Sec. 3.

5. Discussion

Noise simulators for CT images introduce a way to test the accuracy of image analysis methods intended for real

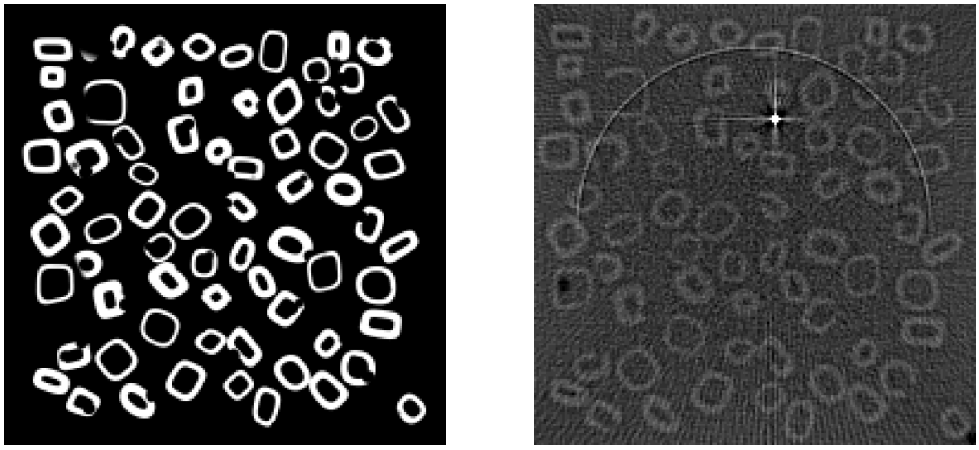

Figure 4. Left: A slice from a synthetic reference volume, i.e. free from noise. Right: The reconstruction of the slice to the left.

data and also allow to study the various types of noise independently from one another.

Our simulator produces μCT images with artefacts that have similar characteristics to those found in real images of composite fibre materials that we have collected at the TOMCAT beamline at PSI. However, it is important to mention that these particular noise levels and artefacts should not be seen as representative for the capabilities of the TOMCAT beamline. In fact some of the artefacts, like the ring artefacts, may be corrected on site during the reconstruction of the volume images if the user asks for it. The goal of our simulator is contrary to that of a good imaging facility. It is to provide realistic but challenging images, corrupted by noise and artefacts, to test the limits of image analysis and processing algorithms. The performance is sufficient for initial needs but future work includes:

- Extending the methods for generation and packing of fibers to mimic a wider range of fiber materials. This includes for instance more entangled fibers, better control of isotropic and anisotropic fiber distributions and the inclusion of damaged fibers and debris.
- A more physically correct simulation of ringing effects due to phase coherence in the beam. A pure phase contrast mode would also be desirable, to complement the current density-based μCT images.
- Including more reconstruction methods and artefact removal techniques, in particular the methods that are actually used in practice at SLS [7] and other facilities.

Preliminary results of the synthetic fibre generation were presented and used in [18]. The current version and planned future versions are focused on the use of simulated μCT data for the validation of algorithms in image analysis and image processing. It is the intention of the authors to make a set of volume images publicly available for scientific use at the project homepage.

Device or option	Comment	Parameters
Detector	Gaussian	$\sigma_{sensor} = 14$
Detector PSP	Gaussian blur	$\sigma_{psp} = 0.35$
Mean Beam Intensity	AR(26)	$\sigma_m = 42$
Beam fluctuations	Gaussian	$\sigma_{beam} = 214.5$
Non-Proportional pixels		$\sigma_p = 0.05$
Reduced FOV		$r_{\text{FOV}} = 10$
Phase effects		$S_p = 0.3$
Bit-Depth of detector	round-off	14-bit
Intermediate storage	round-off	16-bit
Calculations		64-bit double
Number of rays		N_r
Number of projections		$M_p = 0.5\pi N_r$
Matrix absorption		0.7
Fibre absorption		1
Cross section shape		$n \in [2, 4]$
		$r_{1,2} \in [4, 9]$
Wall thickness		$t \in [1.5, 4]$
Fibre length		$L \in [100, 160]$
Fibre rotation		$f \in [0, 2\pi]$
Fibre bending		$R \in [150, 300]$

Table 1. A summary of the parameters.

Acknowledgments

The authors thank Gunilla Borgefors, all partners in the WoodFibre3D project, Federica Marone and Sam McDonald for their assistance during image acquisation and discussions on CT as well as Max Langer for discussions on phase effects. Image data used was obtained at the TOMCAT beam line at the Paul Scherrer Institut, Villagen, Switzerland, proposal 20081028. This work was funded through WoodWisdom-Net under project number 352006A and has been supported by the European Commission under the 6th Framework Programme: Strengthening the European Research Area, Research Infrastructures. Contract no: RII3-CT-2004-506008.

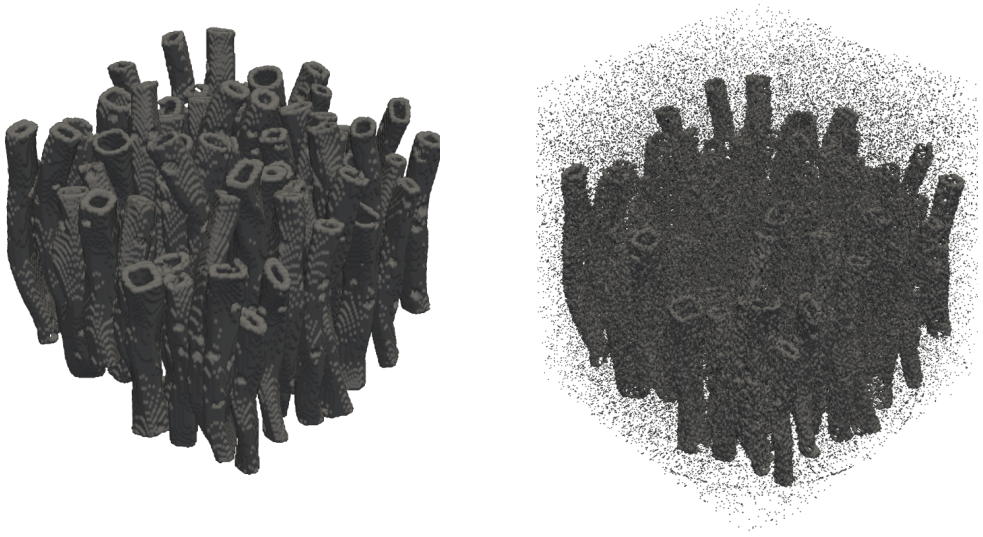

Figure 5. Surface renderings of the synthetic fibre volume using VTK. Left: Before CT simulation. Right: After CT simulation and bilateral filtering.

References

[1] M. Aronsson and G. Borgefors, "2D segmentation and labelling of clustered ring shaped objects", volume Scandinavian Conf. on Image Analysis, pp. 272–79, 2001.

[2] M. Axelsson, "3D tracking of cellulose fibres in volume images", In *IEEE Int. Conf. on Image Processing*, volume 4, pp. 309–312, 2007.

[3] M. Axelsson, S. Svensson, and G. Borgefors, "Reduction of ring artefacts in high resolution x-ray microtomography images", In *DAGM Symposium on Pattern Recognition, Berlin*, pp. 61–70, 2006.

[4] P. Cloetens, M. Pateyron-Salomé, J. Buffière, G. Peix, J. Baruchel, F. Peyrin, and M. Schlenker, "Observation of microstructure damage in materials by phase sensitive radiography and tomography", *J. Appl. Phys.*, 81(9), 1997, pp. 5878–5886.

[5] M. Donoser, T. Mauthner, H. Bischof, and J. Kritzinger, "A probabilistic approach for tracking fibers", In *19th Int. Conf. on Pattern Recognition*, pp. 1–4, Dec. 2008.

[6] S. R. du Roscoat, J.-F. Bloch, and X. Thibault, "Synchrotron radiation microtomography applied to investigatation of paper", *J. of Physics D: Applied Physics*, 38, 2005, pp. A78–A84.

[7] M. S. et al., "Trends in synchrotron-based tomographic imaging: the SLS experience", *Developments in X-Ray Tomography V, edited by Ulrich Bonse, Proc. of SPIE*, 6318, 63180M, 2006, pp. M1–14.

[8] M. Faessel, C. Delise, F. Bos, and P. Castra, "3D modelling of random cellulosic fibrous networks based on x-ray tomography and image analysis", *Composites Science and Technology*, 65(13), 2005, pp. 1931–1940.

[9] A. Kak and M. Slaney, *Principles of Computerized Tomographic Imaging*, IEEE Press, 1999.

[10] H. Madsen, *Time Series Analysis*, Technical University of Denmark, 2nd edition, 2006.

[11] F. Malmberg, J. Lindblad, C. Östlund, K. Almgren, and E. K. Gamstedt, "An automated image analysis method for measuring fibre contact in fibrous and composite materials", In *Proc. of 13th European Conf. on Composite Materials, Stockholm*, 2008.

[12] B. Münch, P. Trtik, F. Marone, and M. Stampanoni, "Stripe and ring artifact removal with combined wavelet – fourier filtering", *Optics Express*, 17(10), 2009, pp. 8567–8591.

[13] K. Perlin, "An image synthesizer", *SIGGRAPH Comput. Graph.*, 19(3), 1985, pp. 287–296.

[14] C. Raven, "Numerical reduction of ring artifacts in microtomography", *Review of Scientific Instruments*, 69(8), 1998, pp. 2978–2980.

[15] S. Svensson and M. Aronsson, "Using distance transform based algorithms for extracting measures of the fibre network in volume images of paper", *IEEE Transactions on Systems, Man, and Cybernetics, Part B*, 33(4), 2003, pp. 562– 571.

[16] S.-J. Tu, C. C. Shaw, and L. Chen, "Noise simulation in cone beam CT imaging with parallel computing", *Phys. Med. Biol.*, 51, 2006, pp. 1283–1297.

[17] H. Wang and S. Shaler, "Computer-simulated three-dimensional microstructure of wood fibre composite materials", *J. of Pulp and Paper Science*, 24(10), 1998, pp. 314–319.

[18] E. L. G. Wernersson, A. Brun, and C. L. L. Hendriks, "Segmentation of wood fibres in 3D CT images using graph cuts", In *Proc. of 15th Int. Conf. on Image Analysis and Processing (in press)*, 2009.